Breakdown of the viscous regime and maximum drag reduction in riblet surfaces

Ricardo García-Mayoral, Javier Jiménez
Grupo de Mecánica de Fluidos Computacional, E.T.S.I. Aeronáuticos
Universidad Politécnica Madrid, Pz Cardenal Cisneros 3, 28040 Madrid, Spain
ricardo@torroja.dmt.upm.es, jimenez@torroja.dmt.upm.es

Summary

The drag reducing properties of riblet surfaces, which reduce turbulent skin friction by up to 10-15%, depending on the particular geometry, are analysed. In the so called viscous regime, for vanishing riblet spacing, the drag reduction produced by riblets is proportional to their size. However, for a riblet spacing $\sim 10^{+}$-20^{+} that depends on the riblet shape, the viscous regime breaks down, and the drag reduction eventually becomes drag increase. Although some work has been done on the breakdown of the viscous regime, its mechanism is not yet fully understood, and the exact spacing for maximum drag reduction can only be determined experimentally. A new length scale is proposed, the groove cross-section A_g^+, for which drag reduction results for different geometries collapse significantly better. To investigate the breakdown of the viscous regime, DNSes with increasing riblet size are systematically conducted. The interaction of the overlying turbulent flow with the riblets and its impact on the drag reduction properties of the ribbed surface are analysed.

1 Introduction

The reduction of skin friction for turbulent flow has been an active area of research in the past decades. Surface riblets are one of the techniques successfully investigated. They are small surface protrusions, or grooves, aligned with the direction of the flow, that confer an anisotropic roughness to the surface. They usually have small sizes. For practical aircraft applications, the optimum riblet separation is of the order of 30-70 μm.

Riblets of very different geometries have been tested with varying results. Walsh and Lindemann [33] performed wind tunnel tests on different riblet shapes, including triangular, notched-peak, sinusoidal, and U-shaped riblets, obtaining a maximum drag reduction of 7–8% for riblet spacings of approximately 15 wall units. Walsh also published an early but quite broad review [32], in which results for various shapes were given. More recent reviews are those of Choi [8] and Bushnell [5]. Riblet experiments have also been conducted in oil and water channels, which allow larger riblet dimensions, and consequently better control of the geometry. Oil channel tests of shark-skin replicas, hairy surfaces, and riblets with adjustable geometry have been conducted by the group led by Bechert *et al.* [4, 3]; they also conducted extensive tests on blade-shaped and trapezoidal groove riblets [2], and proposed the latter as a compromise between optimum performance and practicable fabrication and maintenance. Itoh *et al.* [16] have lately tested the drag reduction ability of seal fur in a water and glycerol channel, obtaining a maximum reduction of 12%.

Concerning the physical mechanism of the riblet drag reduction effect, many experiments have been conducted to observe and analyse the detailed flow field within and above the grooves. Mean and local velocity profiles and turbulent statistics have been reported for experiments both in wind tunnels [31, 27, 23] and water channels [29]. Bechert and Bartenwerfer [1] proposed that the drag reduction is caused by a protrusion height, or offset between the virtual origin seen by the streamwise shear flow and some notional mean surface location. Compared to a smooth wall, this offset would result in a greater separation between the wall and the turbulent streamwise vortices, reducing the momentum exchange at the wall. The correct form of the protrusion height was given by Luchini *et al.* [24], who defined it as the offset between the virtual origins of the streamwise and spanwise flows. Its relation with the drag reduction was given by Jiménez [18] from DNS results.

Several works have analysed the flow structure over riblets from a numeric simulation perspective. Chu and Karniadakis [9] and Choi *et al.* [6] conducted DNSes of turbulent flow over triangular-shaped riblets, obtaining turbulent statistics and skin friction data. Choi *et al.* proposed that the drag reduction worsens for large riblet spacings because vortices tend to lodge inside the riblet grooves. Goldstein *et al.* [13] performed DNS experiments to investigate the drag reduction mechanism, concluding that such reduction is due to the damping of the spanwise velocity by the riblets. Goldstein and Tuan [14] later investigated by DNS the reason why drag reduction worsens for large spacings, concluding that the deterioration is due to a two-dimensional phenomenon in the crossflow; the unsteadiness of the spanwise flow generates secondary streamwise vorticity over the riblets that creates extra dissipation. On the other hand, it is known that spanwise oscillation of the wall, which also presumably introduces unsteady vorticity, decreases drag [21], and that modifying the spanwise boundary condition to inhibit the creation of secondary wall vorticity increases it [17, 20]. The issue therefore remains unresolved.

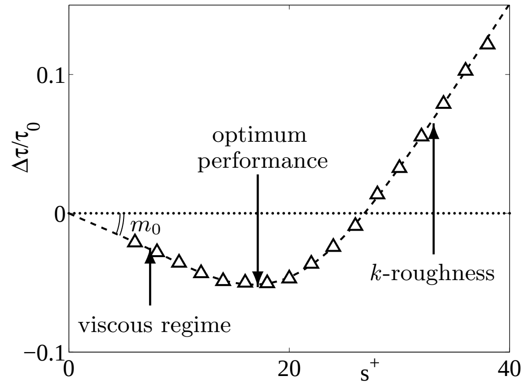

Figure 1: Effect of the peak-to-peak distance, s^+, on the skin friction of a triangular riblet with 60° peak sharpness, from [2].

This paper is organised in two parts. The first one, including Sections 2 and 3, is dedicated to the review of the available experimental data and the conclusions derived from it. Section 2 reviews the different regimes experimentally found for riblet drag reduction and discusses the possible physical mechanisms involved in the breakdown of the linear behaviour. We analyse the viscous regime for very small riblets, its breakdown and the optimum performance of riblets. Section 3 discusses the suitability of the parameters that have traditionally been used to express riblet drag reduction, and propose an alternative set. We find that, when drag reductions are expressed as a function of the groove cross-section instead of the riblet spacing, the points of optimum performance of the geometries reviewed collapse with a scatter below 15%. Using the viscous slope obtained from two-dimensional Stokes simulations, the maximum drag reduction obtainable from a given riblet geometry can then be predicted with an error below 20%. The second part of the paper, covered by Sections 4 and 5, deals with a numerical simulation approach to the understanding of the breakdown of the viscous regime. First we briefly outline the numerical method used for the Direct Numerical Simulation (DNS) of ribbed channels, and give the parameters of the simulations. In Section 5 we present the simulation results, and discuss the relationship between the breakdown of the viscous regime, the riblet geometry and the overlying turbulent flow. We summarise our conclusions in the final section.

2 Drag-reduction regimes for riblets

2.1 The viscous regime

Early in the investigation of riblets, experiments showed that the Reynolds number dependence of their effect on the skin friction could be expressed in large part in terms of the riblet spacing measured in wall units, $s^+ = su_\tau/\nu$, where ν is the kinematic viscosity, and u_τ is the friction velocity [33], typically 2–3% of the velocity outside the boundary layer for aircraft cruise conditions. Figure 1 shows a typical curve of the drag reduction as a function of riblet spacing. For small s^+, the contribution of the nonlinear terms to the flow over the riblets is negligible, and the drag reduction, $DR = -\Delta\tau/\tau_0$, behaves linearly, where τ_0 is the skin friction for the smooth wall. We will denote this regime as 'viscous'. For $s^+ \gtrsim 10$, the drag reduction departs from this linear trend, and eventually turns into a drag increase with respect to smooth surfaces, adopting a typical k-roughness behaviour [19]. The optimum spacing for which drag reduction is maximum is usually $s^+_{opt} \approx 10-20$. Both the slope of the drag curve in the linear region,

$$m_0 = -\left.\frac{\partial(\Delta\tau/\tau_0)}{\partial s^+}\right|_{s^+=0}, \tag{1}$$

and the optimum riblet spacing s^+_{opt}, depend on the riblet geometry, but the qualitative behaviour is always as just described.

In the following, we will call x, y and z to the streamwise, wall-normal and spanwise coordinates, and u, v and w to the corresponding velocity components.

There is a thin near-wall region in turbulent flows over smooth walls in which viscous effects are dominant, and where the mean velocity profile is linear. Its thickness is 5–10 wall units [30], and nonlinear inertial effects can be neglected within it. From the point of view of this layer, the outer flow can be represented as a time-dependent, but otherwise uniform shear. Riblets destroy this uniformity near the wall but, if $s^+ \ll 1$, the flow still behaves as a uniform shear for $y \gg s$. A further simplification is that, since the equations of motion are locally linear, and since the riblet boundary is uniform in the streamwise coordinate and the outer shear varies only slowly with x, when compared with the variations in the cross plane $z-y$, the problem decouples into two parts, both of which are two-dimensional in the cross plane $z-y$. One is the longitudinal flow of u, driven by a streamwise shear

$$u \approx S_1\,(y-\Delta_u), \qquad y \to \infty. \tag{2}$$

The other one is the transverse flow of v and w, driven by

$$w \approx S_3\,(y-\Delta_w) \quad \text{and} \quad v \to 0, \qquad y \to \infty. \tag{3}$$

Far from the wall the effect of the riblets reduces to the virtual origins Δ_u and Δ_w, which are different for the two flow directions. It was suggested in [1, 24] that the offset between those two virtual origins, the 'protrusion height', $\Delta h = \Delta_w - \Delta_u$, was the reason for the drag reduction in the viscous riblet regime. Intuitively, if the cross flow has a higher virtual origin than the longitudinal one ($\Delta h > 0$), the spanwise flow induced by the overlying streamwise vortices is impeded more severely than it would be over a smooth wall. The streamwise vortices are displaced away from the wall, and the turbulent mixing of streamwise momentum is reduced. Since this mixing is responsible for the high local shear near the wall [26], its reduction results in a lower skin friction.

The numerical calculation of Δh is a simple problem, which only requires the solution of two steady two-dimensional Stokes flows: the streamwise and spanwise flows which yield Δ_u and Δ_w. This problem is much simpler, and implies a much smaller computational effort, than the complete problem of simulating the turbulent flow over ribbed walls. It is therefore of great interest to extend the application of Stokes two-dimensional results as much as possible into the riblet drag reducing performance range.

2.2 The breakdown of the viscous regime

As the Reynolds number of the riblets increases, the predictions of the viscous theory, and in particular the linear dependence of the drag reduction with s^+, break down. This is the regime that ultimately limits the practical performance of riblets, and understanding it is therefore important. In particular, if it could be shown that the Reynolds number of breakdown is somehow related to the geometry of the riblet, it might be possible to devise surfaces with critical Reynolds numbers higher than the present ones, and consequently with higher peak performances. We will see in Section 3.2 that there is some evidence for this possibility, but the range of optimum spacings is narrow, and the reason for their variation is, in any case, not understood.

The theories for why the effect of riblets deteriorates beyond $s^+ \approx 10$ fall into two broad groups. One is that their effect on the crossflow somehow loses effectiveness once the flow moves away from the Stokes regime. Reference [14], already mentioned in the introduction, is in that class. They propose that, once the crossflow over the riblets starts separating and shedding small-scale vortices, the extra dissipation appears in the flow as drag. We have also mentioned contradictory evidence, both from unsteady spanwise oscillations of the wall, which decrease drag even if they presumably introduce extra vorticity [21], and from numerical experiments that increase drag by inhibiting the formation of secondary vortices [17, 20]. The message of those experiments could be that introducing small-scale streamwise vorticity at the wall decreases drag by damping the larger streamwise vortices of the buffer layer, and therefore that inertial crossflow effects could be beneficial, rather than detrimental, for drag reduction. The other group of theories assumes that the observed optimum wavelength, $s^+ \approx 10-20$, is related to the scale of the turbulent structures in the wall region. In that group we could mention the observations in [29, 23, 6] that the degradation of the drag reduction coincides with the lodging of the vortices within the riblet grooves. A possibility that did not seem to have been considered in the literature is that the concept of protrusion height could be extended beyond the strictly viscous regime, and that the observed deviations from linearity are due to nonlinearities within, but not necessarily above, the riblets. In that model the flow far from the riblets could still be considered a simple steady shear, but within the riblets it would already begin to feel the effects of the finite Reynolds number. We conducted simulations based on this model [12], obtaining only small variations departing from the viscous protrusion height, of variable sign depending on the riblet geometry and the range of s^+. Changes of the order required to explain the experiments were not reached until $s^+ \approx 20-40$, which is too large.

3 Fundamental parameters for the characterization of riblet drag reduction

3.1 Drag reduction expressed in terms of the shift in the logarithmic profile

The dependence of the drag reduction on the Reynolds number cannot be completely described by the variation of s^+. The classical theory of turbulent boundary layers is that surface manipulations only modify the intercept

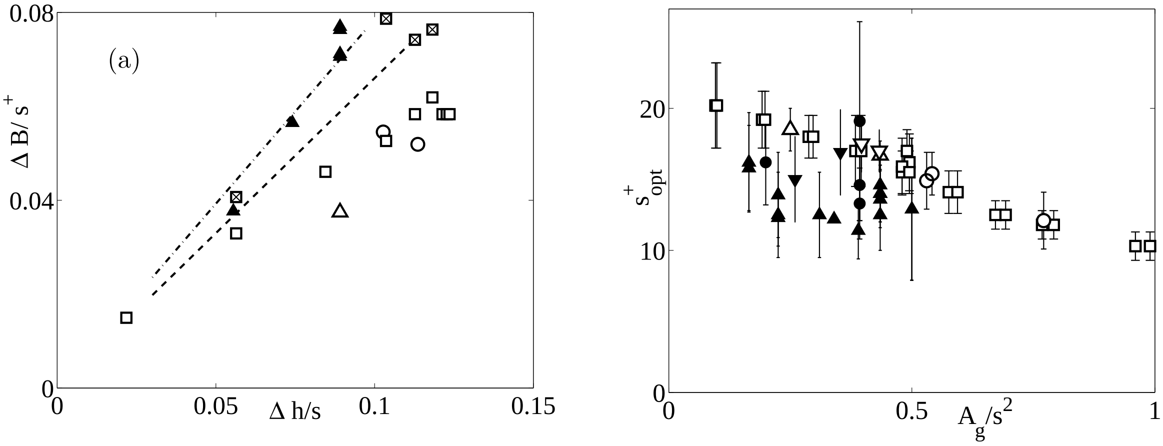

Figure 2: (a) Experimental values of the viscous slope, as a function of the theoretical protrusion height. (b) Riblet spacing for maximum drag reduction, as a function of the relative groove cross section A_g/s^2. △ , triangular riblets; ▽ , notched top and flat valley riblets; ○ , scalloped semicircular grooves; □ , blade riblets. Solid symbols are results from Walsh *et al.* [33, 32], and open symbols results from Bechert *et al.* [2]. ---- , equation (6); −·− , equation (7). Error bars in (b) have been estimated from the drag measurement errors given in the references.

of the logarithmic velocity profile, while both the Kármán constant, $\kappa \approx 0.4$, and the wake function are unaffected [10]. The free-stream velocity can then be expressed as

$$U_\delta^+ = \left(\frac{2}{c_f}\right)^{1/2} = \kappa^{-1} \log \delta^+ + B, \tag{4}$$

where δ^+ is the friction Reynolds number, and B includes both the near-wall intercept and the contribution from the wake. The effect of a given riblet would then be to change B by a given amount, which would be equivalent to the 'roughness function' used to characterise rough surfaces [19]. The resulting change of c_f depends on the Reynolds number δ^+. It follows from (4) that, for constant U_δ and small relative variations of the friction coefficient,

$$\frac{\Delta c_f}{c_{f0}} = \frac{\Delta \tau}{\tau_0} = -\frac{\Delta B}{(2c_{f0})^{-1/2} + (2\kappa)^{-1}}, \tag{5}$$

where the first term in the denominator is due to the change of u_τ in U_δ^+, and the second one comes from the corresponding change in δ^+. Comparison between riblets at different Reynolds numbers should then be done in terms of the roughness function ΔB, not of $\Delta\tau/\tau_0$, and the same should be true when reducing experimental data to aeronautical applications.

The effect of the protrusion height on the displacement of the streamwise vortices away from the wall, mentioned in Section 2.2, can be quantified in terms of ΔB when Δh is given in wall units. Jiménez [18] conducted direct simulations of channels in which the protrusion effect was modelled using the active control approach of [7]. The results were consistent with

$$\Delta B = \mu_0 \Delta h^+ \approx 0.66 \Delta h^+. \tag{6}$$

The above equation agrees well with a rapid-distortion model also in [18], but the coefficient should be treated with care because of the very low Reynolds numbers at which the numerical experiments were conducted. Bechert [2] proposed a different model, based on the modification of the logarithmic velocity profile caused by a virtual origin, according to which

$$\Delta B = \mu_0 \Delta h^+ \approx 0.785 \Delta h^+. \tag{7}$$

The coefficients in equations (6) and (7) are too similar to determine from experimental data which one represents reality more accurately. In any case, the viscous performance of the riblets is given by

$$\frac{\Delta B}{s^+} = \mu_0 \frac{\Delta h}{s}, \qquad s^+ \ll 1, \tag{8}$$

where μ_0 is the coefficient in either (6) or (7), related to the drag-reduction slope m_0 by combining equations (1),(8), and (5) in the limit $s^+ \to 0$,

$$m_0 = \frac{\mu_0}{(2c_{f0})^{-1/2} + (2\kappa)^{-1}} \frac{\Delta h}{s}. \tag{9}$$

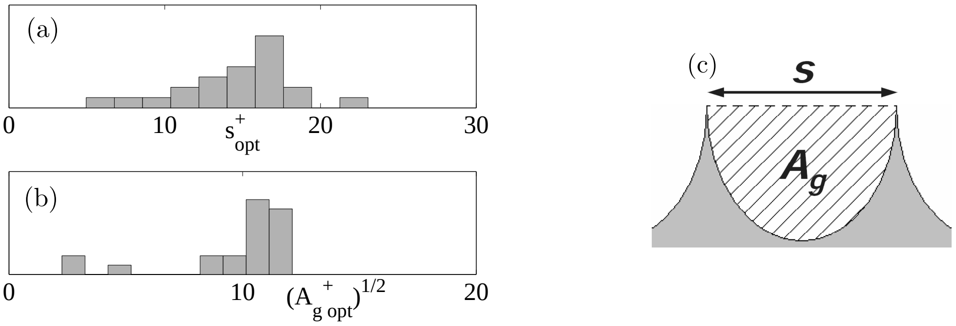

Figure 3: (a) and (b), histograms of the optimum performance point for several riblet geometries, expressed as a function of different geometric parameters. (c) Definition of the groove cross section, A_g.

A compilation of the experimental data available is shown in Figure 2(a), which should be interpreted in the light of the experimental ambiguities. For example, the open squares are blade riblets from Bechert [2]. Those with crosses were mounted on a different base plate than those without them, and they agree better with the theory. Bechert noted the discrepancy, and repeated the second set of experiments after sealing the riblet base. That increased the drag reduction by about 20%, which would bring them in line with the theoretical prediction, but that experimental series was not documented well enough for us to include the correction in the figure. Similar caveats apply to the other riblets in the figure, including those that appear to agree with the theory.

3.2 Drag reduction regimes in terms of the groove cross-section

As we have mentioned in Section 2, it was stated early in riblet literature that riblet drag reduction can be expressed as a function of s^+, so that for a certain optimum spacing, s^+_{opt}, the viscous regime breaks down and the drag reduction is maximum. However, for a given geometry, as s^+ varies so do all other geometric parameters of the surface –when measured in wall units–, so h^+ could for instance have been used instead of s^+ to characterise drag reduction behaviour. The question arises then of whether s^+ is in fact the parameter that determines when the optimum performance is achieved, or whether it is just a parameter that varies as the determining one does. To illustrate how s^+_{opt} varies depending on the riblet geometry, we have plotted in Figure 2(b) the optimum spacing against the ratio of the groove cross-section to the square of the spacing, A_g/s^2. This is roughly equivalent to a depth-to-width ratio for the grooves, and it results in the best data collapse among the several geometric parameters tested. Although s^+_{opt} is always in the range mentioned above, it is clear from the figure that deeper grooves experience an earlier breakdown of the viscous regime, and that their maximum drag reduction is achieved for narrower riblets. The reason for this is unclear. The vortices of the near-wall region have diameters of the order of 20 wall units [22], and it has been reported in [29, 23, 6] that the degradation of the effect of the riblets is associated with the lodging of the vortices within the riblet grooves. However, while this observation qualitatively explains the order of magnitude of s^+_{opt}, it does not explain why the variation of the groove depth affects the value of s^+_{opt}.

In Figures 3(a) and (b) we portray frequency histograms of the maximum drag reduction points of several riblet geometries. The figures show that the optimum point has a significant scatter when expressed in terms of s^+, on the order of 40%. If the characterising parameter is $(A_g^+)^{1/2}$ instead, the scatter is reduced to ~10%, and we have $(A^+_{g\ opt})^{1/2} \simeq 10.7 \pm 1.0$. The data with lower values of $(A^+_{g\ opt})^{1/2}$ correspond to experiments for which either the viscous slope or the optimum performance point could not clearly be defined, such as the measurements for fibers of Bruse *et al.* [4] or those for seal fur of Itoh *et al.* [16], and have thus been left out in Figure 4.

The above result can be used for rough engineering estimations of the optimum performance of conventional riblets in combination with the value of the viscous slope. We need to define a new viscous slope m_0^* for $(A_g^+)^{1/2}$,

$$m_0^* = - \left. \frac{\partial(\Delta\tau/\tau_0)}{\partial(A_g^+)^{1/2}} \right|_{A_g^+=0} = \frac{s}{(A_g)^{1/2}} m_0, \tag{10}$$

so that in the viscous regime $DR = m_0^*(A_g^+)^{1/2}$. Figure 4(a) depicts full drag reduction curves for the range $(A_g^+)^{1/2} \le 20$, for a wide variety of riblet geometries. The good collapse of the data, at least for $(A_g^+)^{1/2} \lesssim 15$,

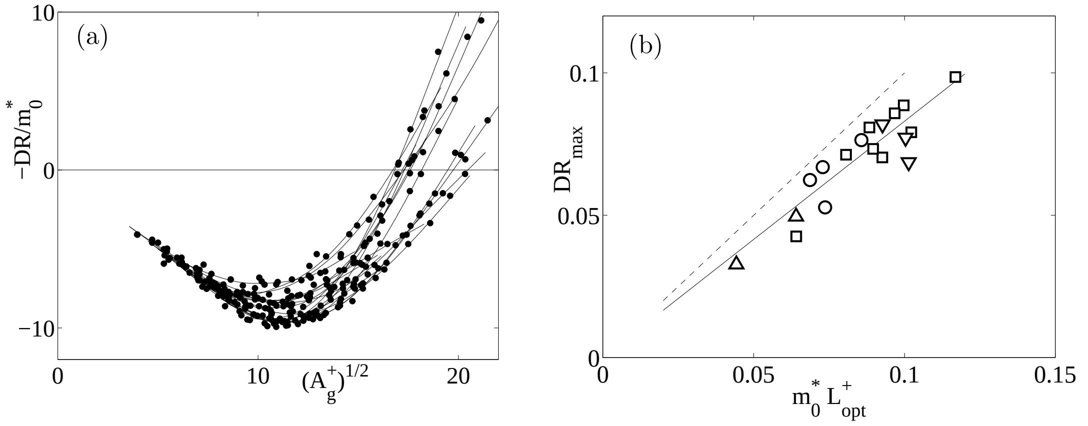

Figure 4: Drag reductions of diverse riblets; (a) Full drag reduction curves from [2], as a function of $m_0^*(A_g^+)^{1/2}$. (b) DR_{max} as a function of $m_0^* L_{opt}^+$; symbols are as in Figure 2; - - - - , extrapolation from the viscous regime; ——— , linear fit with slope 0.83.

Table 1: DNSes parameters.

No. of riblets	0	48	32	24	18	16	15	12
$(A_g^+)^{1/2}$	0	5.06	7.59	10.12	13.50	15.18	17.71	20.25
s^+	0	8.27	12.40	16.53	22.04	24.80	28.93	33.06
$2\pi/L_z$	3	3	3	3	3	3	2.74	3
Re_τ	189.42	185.25	183.77	182.03	182.37	183.63	183.64	188.58

suggests that this Figure can be used, together with m_0^* estimations from viscous computations, as a tool for engineering predictions of drag reduction in a wide range of A_g^+. For the different geometries portrayed, DR_{max} is roughly 83% of the value that would result from the extrapolation of the viscous regime up to $(A_{g\ opt}^+)^{1/2}$. Figure 4(b) portrays the result of substituting the geometry-dependant value of $(A_{g\ opt}^+)^{1/2}$ by a fixed $L_{opt}^+ = 10.7$. The figure shows how the approximation $DR_{max} = .83\, m_0^*\, L_{opt}^+$ is a quite accurate one for conventional riblets, even those with depth-to-width ratios as low as 0.2; the error of the approximation is below 20%. It should however be noted that A_g^+ may not be an adequate parameter to characterise the performance of unconventional geometries, such as the fiber riblets and seal fur that are considered in Figure 3(a) and left out of Figure 4, or the nearly sealed grooves mentioned in [32]; for the limit of fully sealed grooves, the geometry would behave as a flat surface, and modifying A_g^+ would have no performance impact. In any case, the use of $(A_g^+)^{1/2}$ as the characteristic parameter for drag reduction is merely based on the available experimental data, and further insight is needed to justify its use and clarify the nature of the breakdown of the viscous regime. For that purpose, we conduct the numerical experiments described in the next section.

4 Numerical method for DNSes of channels with ribbed walls

In this section we briefly outline the method developed to solve the incompressible Navier-Stokes equations in a parallelepiped domain which includes the walls of a ribbed channel. Rather than imposing strict incompressibility, we impose a rapid convergence of the divergence of the velocity, $D = \nabla \cdot \mathbf{u}$. We substitute the continuity equation with

$$\frac{\partial D}{\partial t} = F\left(D\right) = -\lambda_D D + \frac{1}{\mathrm{Re}_D}\nabla^2 D, \tag{11}$$

where both λ_D and Re_D are positive coefficients. This weak form of the incompressibility condition, similar to that proposed by Nördstrom *et al.* [25], eliminates the usual ‘checkerboard’ problem for collocated grids [11]. The walls of the channel are modeled with an immersed boundary technique [15, 12].

Taking advantage of the periodicity of the problem, the velocity components and the pressure are expanded in Fourier series along x and z, while the spatial differential operators are discretised in y using second-order, centred finite-differences on a non-uniform colocated grid. The grid spacing in y is coarser in the centre of the channel, so that the maximum Δy is $\Delta y_{max}^+ \approx 3$ and the minimum, near the walls, is $\Delta y_{min}^+ \approx 0.3$. The number of x modes is set so that $\Delta x^+ \approx 6$. The number of z modes solved varies for each $x - z$ plane; in the centre of the channel, the modes retained are just enough to capture the smallest turbulent scales, so that

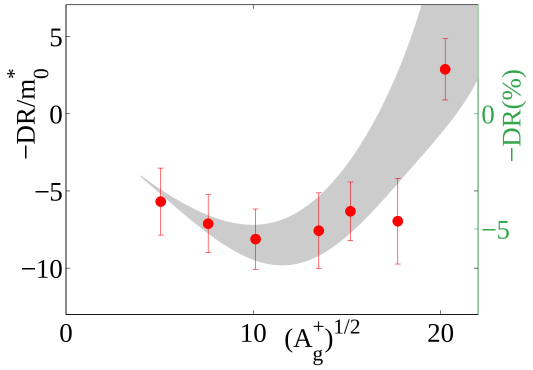

Figure 5: Drag reduction results from DNSes of channels with rectangular riblets. The shaded area envelopes the experimental results shown in Figure 4(b).

$\Delta z^+ \approx 2$, whereas near the channel walls the number of modes retained is larger in order to capture the detail of the immersed boundaries and the adjacent flow. In physical space, the variable number of modes is equivalent to a multi-block arrangement, in which the blocks that include the immersed boundaries have a finer grid in z. Time integration uses a fractional-step, pressure-correction method, in combination with a three-substep Runge-Kutta scheme [28].

We conduct our simulations in periodic channels with streamwise, spanwise and wall-normal dimensions $L_x = 2\pi$, $L_z = 2\pi/3$ and $L_y = 2$. This value of L_y is the distance between the riblet tips at the bottom and top walls; the domain height is slightly larger and adjusted for each test case to contain the whole ribbed surface up to the groove floors. A mean streamwise pressure gradient is imposed to insure constant flow rate $Qx \approx 2$, and the viscosity in the simulations is chosen so $\mathrm{Re}_\tau \approx 180$. We conduct a set of experiments for a variable number of riblets in the box just described, resulting in a set of experiments with different A_g^+. The geometry chosen for our experiments consists of rectangular riblets with aspect ratio $h/s = 0.5$ and blade thickness $t/s = 0.25$. The number of z modes in the blocks containing the riblet surfaces is set so that each riblet spans for 16 grid cells in the spanwise direction, in the dealiased physical space. The parameters of each experiment are given in table 1. Notice that for the case of $(A_g^+)^{1/2} = 17.71$, L_z is slightly increased to obtain the desired A_g^+ while keeping the fixed riblet geometry resolution.

5 DNS results and discussion

Figure 5 portrays the drag reduction obtained from our test cases. The friction coefficients used to calculate the drag reductions in the figure are defined as $c_f = 2/{U_c^+}^2$, where U_c^+ is the time-average of the mean velocity at the central plane for each test case. By choosing U_c^+ instead of the bulk velocity, we seek to obtain friction coefficients whose definition resembles as closely as possible that of friction coefficients in boundary layers, which are based on the free-stream velocity. The friction velocity is estimated from the curve of total stress, $\tau = \tau(y)$, whose time average is nearly linear in y, by extrapolation to a virtual origin defined using a force balance argument. The stress at the walls compensates the pressure gradient driving the flow, which is exerted at the whole channel cross-section. The wall stress is calculated by extrapolation to a fixed y plane which gives the same cross-section. For our rectangular riblets, this origin is $h/4$ above the riblet valleys. Our results show good agreement with the experimental data, represented by the shaded area in Figure 5.

To examine the nature of the flow near the riblet surface, we have conducted statistical analyses of the flow above riblets, which is in average periodic in the riblet spacing. Figure 6(a) portrays the averaged cross-flow inside and immediately above a riblet groove for growing A_g^+. For $A_g^+ = 0$, the viscous two-dimensional cross-flow [12] is shown. For non-zero values of A_g^+, the cross-flow is obtained as a mean of the flow at identical stations above different riblets, over time and over the streamwise coordinate x. Conditioning the average only to y and z would result in a nearly zero secondary flow, so the average is conditioned also to the mean direction of the cross-flow at a plane immediately above the riblet valley, characterising the cross-flow over each riblet groove as ‘rightwards’ or ‘leftwards’. The two statistics of near cross-flow fields are later combined taking into account the existing symmetries. Figure 6(a) shows how for the larger, drag-increasing riblets, the quasi-streamwise vortices are not lodged inside the grooves, as proposed in [6]; Figure 6(b) shows how their distance to the wall decreases slightly for growing A_g^+, but the distance to the riblet peaks is never smaller than $\sim 10^+$. The maximum intensity of the vorticity above the grooves conditioned to the flow direction is about

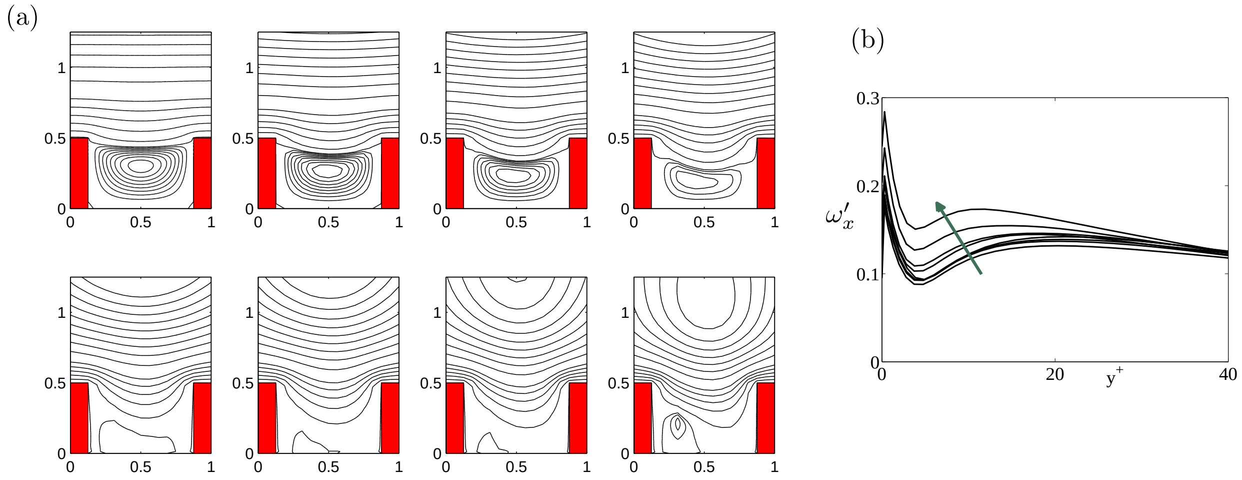

Figure 6: (a) Crossflow streamlines of the averaged flow over and inside the riblet grooves for the test cases in Table 1, for increasing A_g^+. The averaging is conditioned to the direction of the crossflow at a plane immediately above the riblet peaks. (b) Streamwise vorticity fluctuations as a function of the distance to the riblet peak plane. Arrows indicate increasing A_g^+.

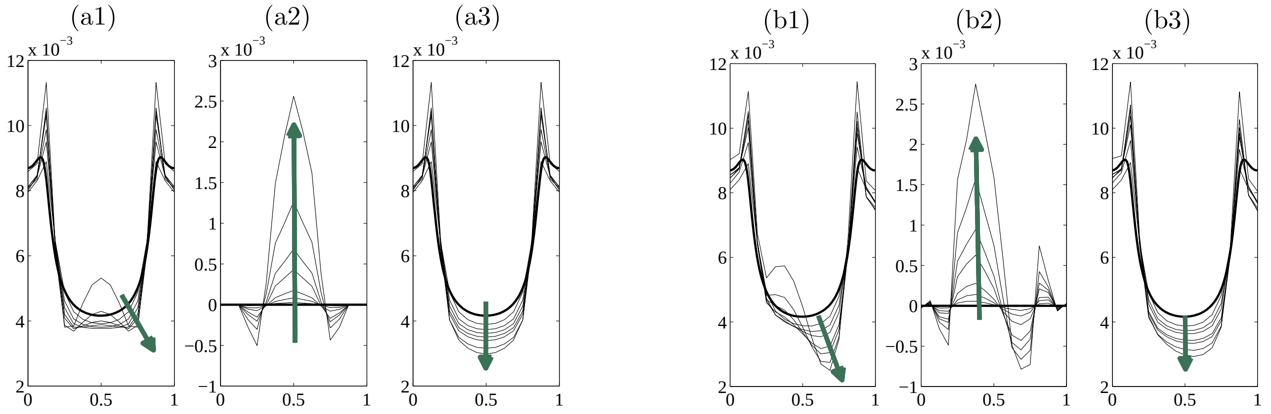

Figure 7: Mean friction stresses at an $x-z$ plane just above rectangular riblets. (a) Not conditioned to the cross-flow direction; (b) conditioned to the cross-flow direction as in Figure 6. (1) Total stress; (2) Reynolds stress; (3) viscous stress. Arrows indicate increasing A_g^+. The highlighted line corresponds to viscous two-dimensional simulations for $A_g^+ = 0$.

one third of the maximum vorticity, suggesting that the overlying vortices are not frozen above the grooves, but instead have a tendency to linger above them more than over the peaks.

Figure 6(a) also shows that, in the viscous regime, a recirculating region exists in the riblet valley. This result was already known from Stokes limit simulations [12], but the new data show the evolution of the recirculating bubble for growing A_g^+, and how it still exists up to the viscous-breakdown region. The recirculating region isolates the valley floor from the overlying flow, preventing the penetration of high momentum flow inside the grooves, and keeping the shear rate low at the groove walls. This low shear inside the grooves is however not sufficient to guarantee drag reduction; for $s^+ \to 0$, the penetration of the outer flow inside the grooves is minimum, but the drag reduction is zero. This is so because the lower shear at the groove walls compensates the high shear at the peaks, so the average friction stress is the same as that of a flat wall. To gain more insight on how the riblet size affects the mean friction stress, and also how the stress is distributed over the riblet geometry, we have computed statistics for the viscous, Reynolds and total stresses at an $x-z$ plane just above the riblet peaks, following a procedure analogous to the one mentioned in the above paragraph. Figure 7 portrays the average stresses, both conditioned and not conditioned to the cross-flow direction. The figure shows how the dominant contribution to the total stress is the viscous stress over the peaks. As A_g^+ increases, the viscous stress increases above the peaks and decreases above the grooves, with a net mean decrease; for the case of the largest A_g^+, the tendency is inverted and the net viscous stress begins to increase. The Reynolds stresses concentrate above the grooves, and are only significant for the larger riblets, for which the recirculation zone has disappeared; in these cases, the increase in the Reynolds stress compensates the viscous stress decrease above the grooves and, for the case of $(A_g^+)^{1/2} \approx 20$, it adds to the viscous stress increase over the peaks to yield a net drag increase.

6 Conclusions

We have reviewed the drag-reduction regimes for riblets, analysing its nature in the viscous limit and exploring the breakdown of the viscous regime. We have analysed how the geometry of the riblets affects that breakdown, and the optimum performance is achieved. We have found that the optima collapse with the parameter $(A^+_{g\ opt})^{1/2}$, which can be interpreted as the characteristic lengthscale of the riblet grooves. In the riblet experiments reviewed, the optimum performance is achieved for $(A^+_{g\ opt})^{1/2} \simeq 10.7$, with a ∼10% scatter. For those configurations, the maximum drag reduction can be predicted with a 20% error if the slope of the drag reduction curve in the viscous regime m_0^* is known. This slope can easily be estimated from simple Stokes flow computations.

We have also analysed the relationship between performance and geometry from numerical simulations. We have observed that the overlying quasi-streamwise vortices concentrate above the riblet grooves, but the vortex lodging proposed in [6] does not occur, at least for $(A^+_{g\ opt})^{1/2} < 20$, which is well past the point of maximum drag reduction, and already into the drag increasing regime. We have found that the breakdown of the viscous regime coincides with the disappearance of the recirculating region in the riblet grooves. Once the recirculation disappears, the Reynolds stresses over the groove become increasingly important, and result in the loss of riblet efficiency and ultimately in a net drag increase.

Acknowledgements

This work was supported in part by the CICYT grant TRA2006–08226, and by the AVERT program of the 6^{th} framework program of the European Commission.

References

[1] D. W. Bechert and M. Bartenwerfer. The viscous flow on surfaces with longitudinal ribs. *J. Fluid Mech.*, 206:105–129, 1989.

[2] D. W. Bechert, M. Bruse, W. Hage, J. G. T. Van der Hoeven, and G. Hoppe. Experiments on drag-reducing surfaces and their optimization with adjustable geometry. *J. Fluid Mech.*, 338:59–87, 1997.

[3] D. W. Bechert, M. Bruse, W. Hage, and R. Meyer. Biological surfaces and their technological application – Laboratory and flight experiments on drag reduction and separation control. *AIAA Pap.*, 97–1960, 1997.

[4] M. Bruse, D. W. Bechert, J. G. T. Van der Hoeven, W. Hage, , and G. Hoppe. Experiments with conventional and with novel adjustable drag-reducing surfaces. In R. M. C. So, C. G. Speziale, and B. E. Launder, editors, *Near-Wall Turbulent Flows*, pages 719–738. Elsevier, 1993.

[5] D. M. Bushnell. Aircraft drag reduction – A review. *Proc. Instn Mech. Engrs*, 217(G1):1–18, 2003.

[6] H. Choi, P. Moin, and J. Kim. Direct numerical simulation of turbulent flow over riblets. *J. Fluid Mech.*, 255:503–539, 1993.

[7] H. Choi, P. Moin, and J. Kim. Active turbulence control and drag reduction in wall-bounded flows. *J. Fluid Mech.*, 262:75–110, 1994.

[8] K.-S. Choi. European drag-reduction research – Recent developments and current status. *Fluid Dynamics Research*, 26:325–335, 2000.

[9] D. C. Chu and G. E. M. Karniadakis. A direct numerical simulation of laminar and turbulent flow over riblet-mounted surfaces. *J. Fluid Mech.*, 250:1–42, 1993.

[10] F.H. Clauser. The turbulent boundary layer. *Advances Appl. Mech.*, 4:1–51, 1956.

[11] J. H. Ferziger and M. Perić. *Computational Methods for Fluid Dynamics.* Springer-Verlag, 1996.

[12] R. García Mayoral and J. Jiménez. On the effect of riblet geometry on drag reduction. *Technical report to the CAFEDA network*, 2007.

[13] D. B. Goldstein, R. Handler, and L. Sirovich. Direct numerical simulation of turbulent flow over a modeled riblet covered surface. *J. Fluid Mech.*, 302:333–376, 1995.

[14] D. B. Goldstein and T. C. Tuan. Secondary flow induced by riblets. *J. Fluid Mech.*, 363:115–151, 1998.

[15] G. Iaccarino and R. Verzicco. Immersed boundary technique for turbulent flow simulations. *Appl. Mech. Rev.*, 56(3):331–347, 2003.

[16] M. Itoh, S. Tamano, R. Iguchi, K. Yokota, N. Akino, R. Hino, and S. Kubo. Turbulent drag reduction by the seal fur surface. *Phys. Fluids*, 18(6):065102, 2006.

[17] J. Jiménez. Wall friction and the structure of near-wall turbulence. In M.R. Davis and G.J. Walker, editors, *11th Australasian Fluid Mech. Conf.*, pages 813–816, Hobart, Australia, 1992.

[18] J. Jiménez. On the structure and control of near wall turbulence. *Phys. Fluids*, 6(2):944–953, 1994.

[19] J. Jiménez. Turbulent flows over rough walls. *Annu. Rev. Fluid Mech.*, 36:173–196, 2004.

[20] J. Jiménez and A. Pinelli. The autonomous cycle of near wall turbulence. *J. Fluid Mech.*, 389:335–359, 1999.

[21] W.J. Jung, N. Mangiavacchi, and R. Akhavan. Supression of turbulence in wall-bounded flows by high-frequency spanwise oscillations. *Phys. Fluids*, A 4:1605–1607, 1992.

[22] J. Kim, P. Moin, and R. D. Moser. Turbulence statistics in fully developed channel flow at low Reynolds number. *J. Fluid Mech.*, 177:133–166, 1987.

[23] S.-J. Lee and S.-H. Lee. Flow field analysis of a turbulent boundary layer over a riblet surface. *Experiments in Fluids*, 30:153–166, 2001.

[24] P. Luchini, F. Manzo, and A. Pozzi. Resistance of a grooved surface to parallel flow and cross-flow. *J. Fluid Mech.*, 228:87–109, 1991.

[25] J. Nördstrom, K. Mattsson, and C. Swanson. Boundary conditions for a divergence free velocity-pressure formulation of the Navier-Stokes equations. *J. Comput. Phys.*, 225:874–890, 2007.

[26] P. Orlandi and J. Jiménez. On the generation of turbulent wall friction. *Phys. Fluids*, 6:634–641, 1994.

[27] S.-R. Park and J. M. Wallace. Flow alteration and drag reduction by riblets in a turbulent boundary layer. *AIAA J.*, 32(1):31–38, 1994.

[28] P. R. Spalart, R. D. Moser, and M. M. Rogers. Spectral methods for the Navier-Stokes equations with one infinite and two periodic directions. *J. Comput. Phys.*, 96(2):297–324, 1991.

[29] Y. Suzuki and N. Kasagi. Turbulent drag reduction mechanism above a riblet surface. *AIAA J.*, 32(9):1781–1790, 1994.

[30] H. Tennekes and J. L. Lumley. *A first course in turbulence.* MIT Press, 1972.

[31] P. Vukoslavcevic, J. M. Wallace, and J.-L. Balint. Viscous drag reduction using streamwise aligned riblets. *AIAA J.*, 30:1119–1122, 1992.

[32] M. J. Walsh. Riblets. In D. M. Bushnell and J. N. Hefner, editors, *Viscous drag reduction in boundary layers*, pages 203–261. AIAA, 1990.

[33] M. J. Walsh and A. M. Lindemann. Optimization and application of riblets for turbulent drag reduction. *AIAA Pap.*, 84–0347, 1984.